



Convection-generated gravity waves in the tropical lower stratosphere from Aeolus wind profiling, GNSS-RO and ERA5 reanalysis

Mathieu Ratynski^{1,a,*}, Sergey Khaykin¹, Alain Hauchecorne¹, M. Joan Alexander², Alexis Mariaccia³, Philippe Keckhut¹ and Antoine Mangin⁴

Correspondence to: Mathieu Ratynski (mathieu.ratynski@estaca.eu)

Abstract. The European Space Agency's Aeolus satellite, equipped with the Atmospheric LAser Doppler INstrument (ALADIN), provides global near-global wind profiles from the surface to about 30 km altitude. These wind measurements enable the investigation of atmospheric dynamics, including gravity waves (GWs) in the upper troposphere and lower stratosphere (UTLS). This study analyzes ALADIN wind observations and ERA5 reanalysis, by deriving GWs kinetic energy (Ek) distributions, examining their temporal and spatial variability throughout the tropical UTLS. A prominent hotspot of enhanced GW activity is identified by Aeolus, migrating from the Indian Ocean in Boreal Summer to the Maritime Continent in Boreal Winter, closely matching outgoing longwave radiation minima and thus highlighting convective origins. Results show that ERA5 consistently underestimates Ek in convective regions, especially over the Indian Ocean, where conventional wind measurements are sparse. Additional comparisons with Global Navigation Satellite System Radio Occultation (GNSS-RO) measurements of GW potential energy (Ep) corroborate these findings and suggest significant underrepresentation of convection-driven wave activity in reanalyses. A multi-instrumental exploratory analysis also allows to verify the empirical grounding of the established Ek to Ep ratio, as well as the wavelength of the waves retrieved by Aeolus. By filling critical wind data gaps, Aeolus emerges as a key tool for improving the representation of GWs, particularly in remote tropical regions. When combined with GNSS-RO measurements, Aeolus data provides new insights into how convective processes drive GW generation, revealing opportunities to refine reanalysis products and model parameterizations, as well as improving the energy ratio.

¹Laboratoire Atmosphère Milieux et Observation Spatiales (LATMOS), Guyancourt, France

²NorthWest Research Associate, Boulder, CO, US

³Program in Atmospheric and Oceanic Sciences, Princeton University, Princeton, New Jersey, United States

⁴ACRI-ST, 260 Route du Pin Montard, Sophia-Antipolis, Biot 06410, France

anow at: Rosenstiel School of Marine and Atmospheric Science, University of Miami, Coral Gables, Florida, United States





1. Introduction

3

4

5

6

9

10

12

13

14

15 16

17

19

20 21

24

25 26

27

29

31

32

2 Atmospheric reanalyses like ERA5, a global atmospheric dataset produced by the European Centre for Medium-range Weather

Forecasts (ECMWF), are essential for climate assessments and atmospheric research. By integrating observational data with

state-of-the-art general circulation models and data assimilation methods, reanalyses provide comprehensive atmospheric

snapshots for a variety of meteorological research (Muñoz-Sabater et al., 2021).

7 However, one significant limitation of these datasets, including ERA5, is their reliance predominantly on temperature

8 measurements for data assimilation, with wind measurements being notably sparse (Campos et al., 2022; Podglajen et al.,

2014). Because of this, ERA5 tends to underestimate low-level wind speeds in certain regions, compared to radiosonde

measurements (Munday et al., 2022). Having said that, only a relatively few radiosonde and cloud-tracked wind measurements

directly constrain wind variability: Radiosonde measurements are notably sparse over oceans, as they are typically launched

from land-based stations, leaving vast oceanic regions under-sampled (Baker et al., 2014; Ladstädter et al., 2011). While some

ship-based radiosonde launches occur, they are infrequent and cover limited areas. Satellite cloud-tracking methods, such as

Atmospheric Motion Vectors (AMVs), provide wind data by tracking cloud movements (Bedka et al., 2009). However, these

methods have limitations: they cannot retrieve wind profiles in clear-sky conditions and often lack detailed vertical resolution.

This results in significant observational gaps in wind measurements over oceans and clear-sky regions. This limitation is

particularly critical when considering atmospheric waves, such as gravity waves, which manifest themselves in temperature

18 and wind vertical profiles.

Gravity waves (GW) play a crucial role in the dynamics of the Earth's atmosphere. Generated by mechanisms such as flow

over orography, convection, and flow deformation, these waves are instrumental in transporting momentum and energy,

22 influencing atmospheric regions far from their origin points (Fritts and Alexander, 2003). While Rossby waves are well

23 represented due to their quasi-geostrophic nature, divergent wave modes like gravity waves, Kelvin waves, Rossby-gravity

waves, and inertia-gravity waves are not sufficiently characterized and must often be parametrized internally by the models

(Plougonven and Zhang, 2014). The underrepresentation of gravity waves with long horizontal and short vertical scales in

ERA5 has been highlighted previously (Bramberger et al., 2022).

28 Furthermore, several studies have identified that the biggest errors in ERA5 reanalysis winds are concentrated in tropical

regions and locations influenced by warm currents, showing that the accuracy of these reanalyses is highly site-dependent

30 (Podglajen et al., 2014; Campos et al., 2022). This is compounded by difficulties in data assimilation systems, such as 4-D var

and perfect model scenarios, which struggle to extract circulation information from high-resolution temperature data (Žagar et

al., 2004). Despite advancements in the quality of tropical forecasts and analyses, the evidence suggests that radio occultation

which requires precise wind profiling.





33 (RO) data could potentially enable effective long-term monitoring of wind fields globally (Danzer et al., 2023). However, the 34 overall lack of direct wind observations continues to pose significant challenges (Baker et al., 2014).

 Historically, most GW studies have relied on ground-based or single-use instruments like radiosondes (Zhang and Yi, 2005), rockets (Wüst and Bittner, 2008), or global coverage measurements from the Global Navigation Satellite System Radio Occultation (GNSS-RO). While GNSS-RO provides high-resolution temperature profiling, effectively characterizing GW potential energy (Ep) (Fröhlich et al., 2007; Khaykin et al., 2015; Schmidt et al., 2016), it does not capture kinetic energy (Ek),

In an effort to bridge many gaps within the observational world, the 2018 launch of the European Space Agency's Aeolus satellite changed our ability to capture atmospheric dynamics, particularly in the upper troposphere and lower stratosphere (UTLS). The UTLS is a region marked by a dramatic increase in static stability at the tropopause, where gravity waves are refracted to shorter vertical wavelengths (Dhaka et al., 2006; Geldenhuys et al., 2023). These short-wavelength waves are primarily lower frequency gravity waves, as dictated by the dispersion relation, and exhibit relatively large amplitude wind variability. This is exactly where Aeolus comes into play: Equipped with its Atmospheric LAser Doppler INstrument (ALADIN), Aeolus is able to measure global wind profiles up to an altitude of 30 km, providing insights into the behavior of gravity waves in these critical atmospheric layers (Banyard et al., 2021; Rennie et al., 2021; Ratynski et al., 2023).

In this context, this study aims at utilizing Aeolus's global wind profiling capabilities to derive a tropics-wide distribution and variability of the kinetic energy of gravity waves, addressing a gap not typically captured in ERA5 reanalysis. By comparing direct measurements with ERA5 data, we reveal certain limitations in the reanalysis's ability to represent tropical gravity wave dynamics. We will look at the most recent reprocessed Aeolus baseline 2B16, providing data from June 2019 to August 2022. Additionally, our study aims at exploring a broader set of analyses, aiming to contextualize the Aeolus wind observations within a multi-instrument framework. By comparing Aeolus-derived kinetic energy of GWs with the potential energy estimates from GNSS-RO, we assess the consistency of independent data sources and examine the ratio of kinetic to potential energy in real-world atmospheric conditions. Beyond energy comparisons, we also investigate the vertical wavelength characteristics of convectively generated waves and discuss limitations that arise from Aeolus' bin settings and instrument-related noise. With this study, we provide the first observational-based three-year tropics-wide climatology of gravity wave kinetic energy and its link with deep convection, identifying source regions for these waves as emanating from tropical deep convection.

The paper will be organized as follows: In Sect. 2, we will discuss the data as well as the methods. It includes a description of the Aeolus, ERA5 and the GNSS-RO datasets, but also explains the horizontal detrending method with its potential and limitations. In Sect. 3, we will analyze the wave activity in terms of kinetic energy using Aeolus Rayleigh wind profiling and directly comparing it with ERA5. Additionally, in Sect. 4, we broaden our analyses to contextualize Aeolus observations against





- 67 GNSS-RO data, criticize the ratio between both elements and determine the wavelength retrieval capability. Finally, the results
- are discussed in Sect. 5, followed by the conclusions in Sect. 6

2. Data and Methods

69

70

82

84

85

8687

88

89

90

91

92

93

94

95

96

2.1 Instruments and Datasets

71 The Aeolus satellite, with its ALADIN Doppler wind lidar, orbited Earth at a 97-degree inclination and 320 km altitude. Its 72 data consists of 24 vertical range bins that divide the atmosphere (Rennie and Isaksen., 2020), allowing wind profiling between 73 0 and 30 km. Laser pulses and two receivers—Rayleigh and Mie channels—detect the atmosphere's Doppler shifts through 74 molecular and particle backscatter, respectively. The data, organized into atmospheric scenes, cloudy or clear (Rennie and 75 Isaksen, 2020), has an 87 km along-track integration and a vertical resolution varying between 0.25 to 2 km. The distribution 76 of these range bins is determined by a dedicated range bin setting (RBS), which can be adjusted to cater to specific needs, such 77 as enhanced sampling at certain heights. This study uses the Level 2B Rayleigh clear product, with the latest Baseline 2B16 at 78 the time of submission, offering the horizontal line of sight (HLOS) wind components. The HLOS wind speed is derived using 79 Aeolus NWP Impact Experiments guidance (Rennie and Isaksen., 2020), with the vertical wind speed assumed to be negligible. 80 The angle θ denotes the azimuth of the target-to-satellite pointing vector, being around 100.5° over the tropics. When injecting 81 the azimuth value into Eq. 1, it becomes apparent that the HLOS wind over the tropics is quasi-zonal.

83
$$v_{HLOS} = -u \sin(\theta) - v \cos(\theta)$$
 (1)

The ERA5 reanalysis dataset, a European Centre for Medium-Range Weather Forecasts (ECMWF) product, offers comprehensive atmospheric, land-surface, and ocean-wave parameters at hourly resolution and global coverage (Hersbach et al., 2020). Its exceptional horizontal resolution of approximately 33 km at the equator (corresponding to 0.3° latitude/longitude), the best among widely used reanalysis products, enables it to resolve gravity waves with horizontal wavelengths as small as ~100 km (Wright and Hindley, 2018, their table 1). Additionally, its higher vertical resolution in the troposphere, with 137 vertical levels reaching up to 0.01 hPa, makes it particularly adept at capturing gravity waves with vertical wavelengths down to ~1–2 km. ERA5 also incorporates advanced modelling features such as sponge layers and hyperdiffusion to attenuate artificial wave reflections and stabilize the model numerically, allowing for efficient modelling of large-scale phenomena, notably simulating gravity waves with wavelengths greater than 400 km (Stephan and Mariaccia, 2021). It is therefore a very strong candidate to use as a benchmark for Aeolus' performances. For this study, wind components are retrieved on standard model levels and converted to specific altitude levels using geopotential height, temperature and humidity.



97 98

99

100

101

102103

104

105

106

107

108

109

110

111

112

113

114



The GNSS-RO method offers many advantages for studying atmospheric dynamics, particularly GW activity and parameters (Tsuda et al., 2000; Fröhlich et al., 2007; Wang and Alexander, 2010; Luna et al., 2013; Schmidt et al., 2016). The Radio Occultation Meteorology Satellite Application Facility (ROMSAF) provides global GNSS-RO datasets, which offer valuable information on atmospheric refractivity, temperature, and geopotential height with high vertical resolution. These datasets are derived from the bending angles of GNSS signals as they pass through the Earth's atmosphere and are observed by low Earthorbiting satellites. It provides global coverage with a high vertical resolution, sub-Kelvin accuracy, full diurnal coverage, and all-weather capability. RO's vertical resolution ranges from 100 meters in the lower troposphere to 1.4 kilometers in the upper stratosphere, with a horizontal resolution of around 300 kilometers. MARQUARDT and Healy (2005) showed that small-scale fluctuations in dry temperature RO profiles could be attributed to GWs with vertical wavelengths equal to or greater than 2 kilometers. Alexander et al. (2008b) suggested analyzing data below 30 kilometers in altitude to maintain the signal-to-noise ratio for temperature fluctuations above the detection threshold, which also happens to be Aeolus' maximal capability. Most GW parameters can be derived from single RO temperature profiles. However, estimating momentum flux requires knowledge of the horizontal wave number or wavelength, which cannot be deduced from a single temperature profile. To determine the horizontal structure of GWs, it is necessary to analyze clusters of three or more profiles adjacent in space and time. The first applications of RO measurements for studying GW activity date back to the early 2000s, and several missions have since provided data for further global GW activity studies (Tsuda et al., 2000; Fröhlich et al., 2007; Wang and Alexander, 2010; Luna et al., 2013; Schmidt et al., 2016). These studies have focused on potential energy as a proxy for estimating GW activity.

Although Aeolus' full operational lifespan spans from August 2018 to April 2023, at the time of this study, the entire dataset has not yet been reprocessed, requiring significant effort from the responsible team. Meanwhile, we focus on the most recent reprocessed Aeolus baseline, 2B16, which covers the period from June 2019 to August 2022. This baseline represents the most up-to-date dataset available and demonstrates the highest fidelity among all previous baselines. Since ERA5 and GNSS-RO have been operational for much longer and remain in use today, we limit the scope of our study to align with the 2B16 baseline

120 period.

This study specifically utilizes Aeolus Level 2B Rayleigh clear HLOS winds, ERA5 wind components, and GNSS-RO temperature profiles, all brought to a standard interpolated grid to facilitate the accurate comparison and integration of data from the different sources. The chosen grid has a vertical resolution of 500 meters and spans a range from 0 to 30 km altitude. This choice of resolution is close to the dataset's (280 m for ERA5, ~300m for GNSS-RO and 1 km for Aeolus) native resolution in the UTLS and serves as an acceptable middle ground.

126127

128

129

130

121122

123

124125

The choice to compare Aeolus measurements directly with ERA5, instead of operational Integrated Forecasting System (IFS) analyses that assimilate Aeolus winds, is intentional. This comparison method distinctively highlights ERA5's limitations in capturing elements of the gravity wave spectrum. By contrasting Aeolus data with ERA5, the study demonstrates Aeolus's





unique contributions and potential to enhance future reanalyses and forecasting models. While operational IFS analyses assimilating Aeolus winds would showcase improved analytical quality, such an approach would obscure the specific enhancements brought by the satellite, blending them with the inherent model capabilities

2.2 Methods and Limitations

The following section discusses the retrieval of GW kinetic energy, Ek. The retrieval faces challenges separating large-scale processes, like gravity, Rossby, and Kelvin waves, from the smaller scale gravity waves.

Several methods exist for background state determination and large-scale process separation, falling into two distinct categories: Either Vertical Detrending (VD), which can be applied to any type of data set, including local observations such as lidars and radiosondes (Gubenko et al., 2012; Khaykin et al., 2015) or Horizontal Detrending (HD), which also encompasses a temporal detrending component, requiring spatially resolved data set, i.e. satellite observations or model reanalyses (Alexander et al., 2008a; Khaykin et al., 2015). A study has discovered significant discrepancies in Ep magnitude when comparing different data sets using these methods (John and Kumar, 2013). Indeed, VD method may remove GWs with long vertical wavelengths whilst retaining short vertical wavelength planetary-scale waves like Kelvin waves, which have been observed with vertical wavelengths as short as 3 km (Alexander and Ortland, 2010; Cao et al., 2022). Furthermore, Schmidt et al. (2016) strongly recommend using HD, as VD may overestimate gravity wave activity due to remnant signals from synoptic and planetary waves and their small vertical scale in the tropics. In our case, the method we propose (computation of background profile for a fixed spatiotemporal grid), falling into the HD category, is best suited for retrieving energy information from Aeolus and ERA5 model reanalysis.

The separation of the wind profile into a background state and perturbations through HD focuses on scales characteristic of gravity waves, thereby filtering out larger-scale processes like Kelvin and Rossby waves. This selection criterion is based on both the scale and structural characteristics of the perturbations. The frequency and wavelength of these perturbations are also critical identifiers of gravity waves, distinguishing them from other atmospheric phenomena.

Moreover, our approach utilizes high-pass filtering techniques, targeting specific frequency or vertical wavelength ranges (7km in Alexander et al. (2008b) and 9km in this study), to further ensure that the perturbations derived from the background profile predominantly represent gravity waves. This method has been widely used for retrieval of GW Ep (Alexander et al., 2008a; Schmidt et al., 2008; Šácha et al., 2014; Khaykin et al., 2015), and Aeolus now provides the necessary tools to apply the same approach for GW Ek.



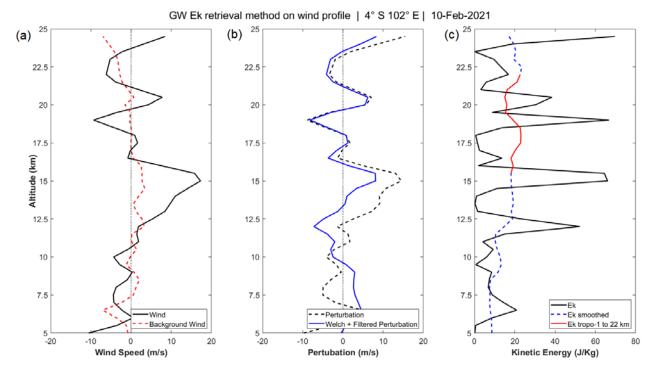


Figure 1. Derivation of GW energy profiles from wind measurements (a) Observed wind profile and the corresponding background state profile. (b) Wind perturbation profile alongside its filtered counterpart. (c) Resulting in Ek, smoothed and then averaged within the given altitude range.

Based on the linear theory of GW, the measured wind profile U(z) shown in Fig.1a is divided into a background wind $\overline{U}(z)$ also present in Fig.1a and a perturbation U'(z) depicted in Fig.1b. The background is obtained by averaging all individual wind profiles for kinetic energy retrieval, within a spatiotemporal grid box of 20° longitude \times 5° latitude over 7 days. Following the arguments presented in Alexander et al., (2008b), this choice is justified by the need to ensure a sufficient number of profiles per grid cell, which minimizes random noise while preserving meaningful variability in the data. Shorter temporal windows would lead to insufficient sampling, while longer windows would smooth out critical small-scale wave features. The grid size is also designed to preserve the spatiotemporal variability of mesoscale gravity waves and equatorially trapped structures, making it possible to separate the background and perturbation components without introducing significant biases. Finally, this configuration mitigates errors in the definition of the $\overline{U}(z)$ profile, ensuring reliable kinetic energy calculations and robust separation of gravity wave perturbations. The average number of profiles used for the background state determination is 55 for Aeolus, 20 for GNSS-RO and 1400 for ERA5.

The next step involves subtracting the background profile from its corresponding individual profile, eliminating most large-scale waves (Planetary Waves, Kelvin Waves, Rossby Waves). This yields the perturbation profile U'(z), which is then subjected to Welch-windowing, which is done in order to mitigate spectral leakage (Alexander et al., 2008a; 2008b; Khaykin



192

197

205

206

207208

209

210

212



et al., 2015). A prior study also applied a similar windowing function (half cosine), aiming to counteract the "effects of the edge of the height range" (Hei et al., 2008). After said windowing, a vertical high-pass filter with a cut-off at 9 km is applied to the perturbation profile, as seen in Fig.1b and 1c.

The highpass filtering is a step that could be considered optional depending on the spectrum of waves studied. Short vertical scale waves in the tropical tropopause layer (TTL) region are particularly interesting due to their influences on thin cirrus and stratospheric dehydration, and their potential role in driving the Quasi Biennial Oscillation (QBO) in the lowermost stratosphere (Kim and Alexander, 2015; Bramberger et al., 2022). Their smaller scale relative to larger atmospheric waves justifies the use high-pass filtering step and are the main cause for this choice. The GW Ek can be derived from the variance of wind components as follows:

191
$$E_k = \frac{1}{2} \left(\overline{u'^2} + \overline{v'^2} + \overline{w'^2} \right),$$
 (2)

where u, v, and w represent the zonal, meridional, and vertical wind components, respectively. However, in our case, since the vertical wind speed is neglected and the satellite is not able to distinguish between zonal and meridional wind, it is necessary to provide a new formalism for the retrieved metric:

196
$$E_{k HLOS} = \frac{1}{2} \left(\overline{v'^2}_{HLOS} \right)$$
 (3)

The resulting profile, which is essentially the perturbation squared, is cut to keep the data between one kilometer below the tropopause and 22 km. The altitude range is chosen considering Aeolus' limitations, such as increasing error at higher altitudes due to lack of backscatter signal (Ratynski et al., 2023, their Fig.3). The lower bound is set one kilometer below the tropopause to focus on events extending beyond it, balancing Aeolus' resolution with our interest in upper-end dynamics. The tropopause is latitude-dependent and determined using NCEP reanalysis, which provides results similar to ERA5 but is more accessible and easier to integrate. The profile is then smoothed using a 14-point moving average over the 49-point profile and finally averaged over its total length, representing the Ek, as seen in Fig.1c.

Although the above steps focus on retrieving GW Ek from Aeolus wind measurements, the same procedure can be applied to temperature-based observations such as GNSS-RO for Ep. The main difference lies in substituting temperature T(z) for wind U(z) throughout the background-perturbation decomposition, which means using T'(z) rather than U'(z). The same low-pass and high-pass filtering strategy, windowing (e.g., Welch or half-cosine), and vertical averaging steps then provide the Ep profile from the temperature perturbations. In this case, the GW Ep is calculated using this formula:

$$211 E_p = \frac{1}{2} \left(\frac{g}{N}\right)^2 \left(\frac{T'}{\bar{T}}\right)^2 (4)$$





Where the Brunt-Vaisala frequency squared (N2) is smoothed using binomial (Gaussian) smoothing of 10th order.

Consequently, the data treatment across various instruments, whether wind or temperature remains consistent.

Since our study focuses on the tropical UTLS region, the meridional wind component will have a minor contribution compared to the zonal component. Therefore, the $E_{k\ HLOS}$ energy represents primarily the zonal activity, meaning that we are missing a non-negligible proportion of wave activity. To evaluate the contribution of v' to the total kinetic energy we use ERA5 data and compute the ratio between total Ek (derived from u' and v') and $E_{k\ HLOS}$ (as it is observed by ALADIN).

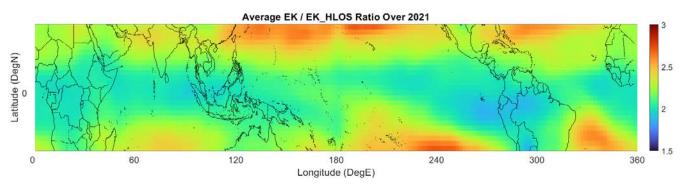


Figure 2. Temporal and spatial variability of the ratio between E_{kHLOS} and Ek in the ERA5 model over the tropical region (30°S–30°N) for the year 2021

Figure 2 displays the ratio between $E_{k \; HLOS}$ and Ek in the ERA5 model, over the tropical region for the UTLS. The ratio values range from 1.5 to 3, between January 2021 and December 2021 included, depicting variations in how well the HLOS measurements capture the total kinetic energy in this region.

We specifically selected the year 2021, a period characterized by high energy levels in the Aeolus dataset. However, this choice does not significantly affect the spatial distribution of the ratio, as the overall patterns remain consistent year to year (the projection is always the same). By focusing on a single year, we aim to highlight the most prominent features of the ratio without averaging out key differences.

In general, the degradation of the Ek ratio as we move away from the equator is evident, aligning with theoretical expectations based on Eq. 1. For example, over the Indian Ocean, robust and persistent easterly trade winds align well with Aeolus' line-of-sight direction, keeping the ratio relatively low at around 1.5. In contrast, over regions with more meridionally oriented circulations, such as parts of the American continent during certain periods, Aeolus captures less of the total kinetic energy due to the weaker zonal flow, pushing the ratio upward. Over the equatorial band (10°S–10°N), the ratio exhibits notable regional variations. In the western Pacific (120°E–180°E), the ratio remains relatively stable, fluctuating between 1.6 and 1.9 for this specific year, suggesting that a significant portion of the zonal wind energy is captured by Aeolus in this region. In





(5)

contrast, over the American continent (240°E–300°E), the ratio increases significantly, reaching values up to 2.6, indicating a greater influence of the meridionally propagating GWs. Meanwhile, over the Indian Ocean (60°E–120°E), the ratio is lower, around 1.5 to 1.6, implying that a larger fraction of the total kinetic energy is captured by Aeolus, due to the predominance of the zonal tropical trade winds in this region.

When these values are averaged over the years of the mission, the overall patterns remain similar, but with slightly different magnitudes. Over the western Pacific, the ratio tends to settles at 1.6, while the American continent displays a higher ratio, averaging closer to 2.8. The Indian Ocean shows the lowest ratios, typically around 1.5 in long-term averages, with the lowest values reaching as low as 1.2, further supporting the idea that the zonal wind predominance in this region allows Aeolus to capture a greater share of the total kinetic energy.

When averaged over the entire mission and focused on the equatorial band, the ratio settles at approximately 1.6. This implies that Ek_{HLOS} accounts for around 62.5% of total Ek, the remainder being undetectable due to HLOS projection. The meridional component, less significant in this specific geographical area for Aeolus, contributes the remaining 37.5% of Ek not considered by Ek_{HLOS} . Although not dominant, Ek_{HLOS} represent a substantial contribution to Ek.

Thanks to the given instruments and methods, we can predict both the horizontal and vertical wavelength range of the observations. Aeolus' RBS determines the spacing between sampling points, impacting the vertical and horizontal resolution and maximal detectable wavelength. For vertical wavelengths, the maximum detectable limit with Aeolus is approximately 9 km, roughly half the average profile length in the tropics, after limiting the profile to the optimal range and especially considering the dynamic lower bound. Profiles generally extend to heights between 23km and 26km. The windowing function, along with the high-pass filter, will also dampen the dominant wavelength. In the horizontal dimension, since a 20° x 5° degrees grid is used for the background removal and the wind is supposed quasi-zonal, the zonal wavelengths, therefore, reside below 2220 km.

Additionally, Aeolus can be prone to errors alternating the quality of wind profiles. Amongst the most notable ones are dark currents in the charge-coupled devices ("hot pixels"), potentially leading to errors of up to several meters per second (Weiler et al., 2021). Another identified issue is the oscillating perturbations, parasitic deformations of the signal, yet to be attributed to a cause, which can be mistaken for GW-induced signals (Ratynski et al., 2023). While corrections were implemented for the first issue (Weiler et al., 2021), the overall signal random error varies with time, with a general tendency to increase due to instrument degradation. Aeolus' HLOS wind variance is inherently linked to the measurement noise (i.e., random error). In other words, the observed wind variance is a sum of the variance due to waves (detected using the given data and method) and the variance due to ALADIN noise, i.e., its random error squared.

272 the variance due to ALADIN noise, i.e., its random error squared.

273 $\overline{v'^2}_{HLOS} = \overline{v'^2}_{GW} + \overline{v'^2}_{LN}$





276

277278

279

280

281

282283

284

285286

287

with $\overline{v'^2}_{GW}$ representing the variance contribution from gravity waves and $\overline{v'^2}_{I,N}$ the contribution from instrument noise. The instrument-induced variance can be estimated using collocated reference measurements, which are very sparse and may lack representativeness, or using global meteorological data independent of ALADIN, such as ERA5. The second method was chosen, as ERA5 allows reducing geo-temporal biases compared to fixed sites. While the ALADIN random error exhibits some variability across the tropics, observed fluctuations remain within approximately $\pm 30\%$ (Borne et al., 2024; Ratynski et al., 2023). This degree of variability is considered acceptable, as the correction is applied as a zonal average, effectively smoothing out localized deviations. Another important assumption is that ERA5's random error does not vary with time. These calculations are realized within the $10^{\circ}\text{S}-10^{\circ}\text{N}$ latitude band. The defined meshing for the estimation is 3 weeks, meaning that for each bin, a time averaging will be applied. The values are zonally averaged, which signifies that an average of longitudinal values is calculated for each latitude bin, a process illustrated by placing a cap over the terms. With this, ERA5 can provide independent energy values and is, therefore, able also to estimate the instrument-induced variance and its time evolution. However, the estimations must be done in terms of Ek, as other metrics (such as wind or perturbation) cannot be linked between

$$\overline{Ek_{I.N}} = \overline{Ek_{Aeolus\,HLOS}} - \overline{Ek_{ERA5\,HLOS}}$$
 (6)

289 Where

both datasets:

$$\overline{Ek_{Aeolus\,HLOS}} = \frac{1}{2} \, \overline{v'^2_{HLOS}} \tag{7}$$

291

- 292 By subtracting the Ek instrument noise (being the mean difference between Aeolus and ERA5 Eks for each bin), we impose
- 293 ERA5's average Ek values onto Aeolus' Ek, therefore only leaving the physical signal, with a stable value over the entire
- 294 lifecycle:

$$\overline{Ek_{Aeolus\ HLOS^*}} = \overline{Ek_{Aeolus\ HLOS}} - \overline{Ek_{I.N}}$$
(8)

- With $Ek_{Aeolus\ HLOS*}$ representing the corrected Aeolus HLOS Ek. The correction values fluctuated from 5 J/kg in 2018 and
- 297 2019 to between 10 J/kg and 17 J/kg for the rest of the period, peaking at 23 J/kg in November 2021.

298

- One remark that can be made is that the ERA5 dataset is used to both calibrate $Ek_{Aeolus\,HLOS}$ and as a comparison to $Ek_{Aeolus\,HLOS*}$, which could be considered questionable. While it should, in principle, be better to use the derived noise contribution from an earlier study (Ratynski et al., 2023), relying on a singular-sounding site introduces geospatial biases because of the absence of a global perspective. Applying a site-specific correction to an entire longitudinal dataset might compromise the integrity of the results. Furthermore, the idea of utilizing multiple-sounding sites is constrained by the limited
- 304 availability of such sites, especially in the tropics.





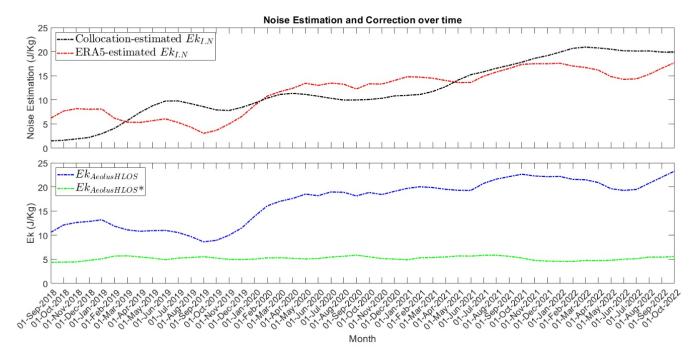


Figure 3. Difference between the Radiosonde-derived (black) and ERA5-derived (red) estimated noise correction, resulting in the difference between the uncorrected Aeolus HLOS GW Ek (blue) and the ERA5-corrected Aeolus HLOS GW Ek (green).

Figure 3, displaying both correction approaches (Site-based on top and model-based on the bottom), is intended to demonstrate that such a method of instrumental noise estimation is qualitatively consistent with the classical approach based on collocated reference measurements applied in (Ratynski et al., 2023).

The Météo-France upper-air soundings in La Réunion (Aéroport Gillot) was used for the conduct of this analysis. For each collocated radiosonde profile with an Aeolus overpass (within 200 km and +/- 6 hours), we downsampled the radiosonde profile resolution to be equivalent to ALADIN vertical bins. A point-wise difference is then calculated, and the standard deviation of these differences is what we refer to as random error. In principle, if Aeolus would not experience any degradation through its systems, this standard deviation would remain stable over the years and periods. However, since we observe an increase, as reported by Ratynski et al. (2023, their Fig.6), a link can be made between the instrument degradation and this increase, wrongly attributing signal-to-noise. Squaring this noise estimation provides a metric homogenous to the observed Ek, representing the repercussions of noise on Ek estimation:

320
$$\operatorname{Ek_{LN}} = \frac{1}{2} \left(\sigma_{\text{Aeolus-Radiosondes}} \right)^2$$
 (9)

While both methods provide similar trends, the model approach remains the safest estimation when considering the potential biases.





325 **3. Results**

326

327328

329

330

331

3.1 Seasonal variation of GW Ek

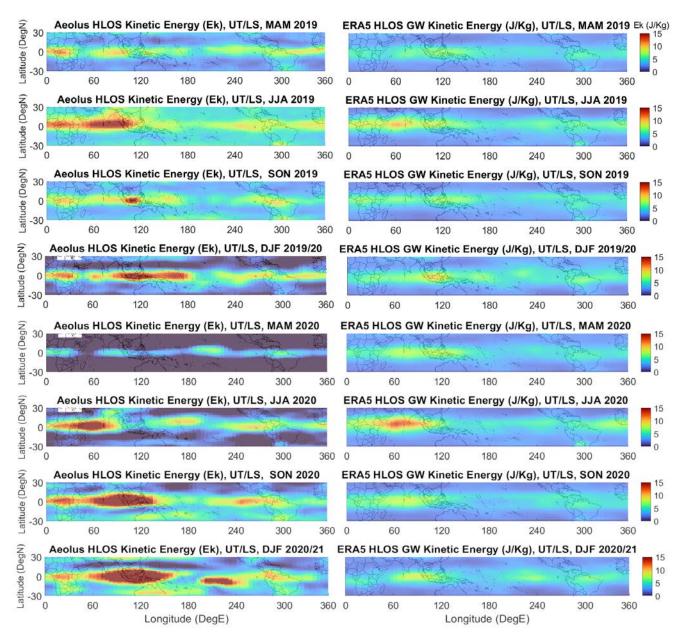


Figure 4. Comparison between $Ek_{Aeolus\ HLOS*}$ (left column) and $Ek_{ERA5\ HLOS}$ (right column). Each line corresponds to a season, from March-April-May 2019 to December-January-February 2021. The white bins represent the lack of satellite information. The UTLS altitudes are defined between one kilometer below the tropopause and 22 km. The tropopause is determined from the NCEP reanalysis.





Figure 4 displays the Ek_{HLOS} distribution from the Boreal Spring of 2019 to the Austral summer of 2020. This represents the first attempt at an observation-based distribution of Ek from GWs in the tropics. From both Aeolus and ERA5 points of view, several recurrent and other dynamical spots can be observed. A notable hotspot over the Indian Ocean in JJA likely relates to Indian Monsoon convection, dissipating by SON. This region is known to have frequent convective events generating many GW activity (Holloway and Neelin, 2007).In DJF, a new hotspot is seen over the Western Pacific and Maritime Continent. There is year-round increased activity over the African continent, probably due to continental convection and higher than average values over the Maritime Continent. More generally, the exhibited Ek activity predominantly lies within the 10° N/10° S boundary. Aeolus's alignment with ERA5 is notable, not only in terms of value but also in distribution and evolution. Furthermore, a previous study using Ep have reported observations similar to ours: the patterns resemble the findings from Alexander et al. (2008b, their Fig.3 and Fig.4), highlighting the same locations and general hotspot distribution. The GNSS-RO derived Ep values, which range from 0 to 6.6 J/kg at 15 km and 0 to 4.4 J/kg at 22 km (Alexander et al., 2008c), after applying the usual Ek/Ep ratio of 1.6, are closely aligned with our observations. This study is independent regarding the datasets and metrics analyzed, adding another layer of confidence.

In contrast to the earlier period, the comparison between Ek_{Aeolus HLOS*} and Ek_{ERA5 HLOS} from March 2020 to February 2021 presents a significant deviation. This is a period of time when La Nina conditions developed, particularly for the SON to DJF period in 2020, leading to increased precipitation in the Maritime Continent region. This climatic phenomenon can partially explain the observed differences between the 2019 and 2020 data for these seasons. A noticeable disparity arises in the energy levels, with Aeolus consistently exhibiting a greater degree of energy compared to ERA5. This discrepancy is not limited to specific seasonal dynamics but pervades across the entire year. The geographical distribution and evolution of energy hotspots are largely similar between the two datasets; however, the intensity and scale of these hotspots are invariably higher in Aeolus.

In JJA, the hotspot over the Indian Ocean previously seen in both Aeolus and ERA5 becomes more pronounced in the Aeolus data, while ERA5 shows a considerable reduction. By SON and DJF, the disparity reaches its peak, the energy in Aeolus remains high, with the hotspot over the Indian Ocean and Maritime Continent becoming even more pronounced. Despite the same general pattern in ERA5, the energy level is notably lower. Starting from DJF 2019/2020, a marked difference is observed between hotspots and other areas. This period coincides with a notable increase in the satellite's random error (Ratynski et al., 2023, their Fig.6), impacting the noise correction approach and leading to an overestimation of variations in high-variability regions, while minimally affecting low-variability areas. Consequently, this translates into altered background levels in the dataset. These observations underline a stark contrast between both datasets, in which Aeolus demonstrates a consistently higher level of energy.

One prominent constant across all periods is the high-energy activity over the African continent. This feature remains consistent regardless of the season or the year, implying a persistent mechanism likely associated with the continental





convection processes that are typical for this region. The other hotspots, however, display more variability. While they maintain their general locations across different seasons, the intensity of energy at these hotspots is subject to significant changes. This variability is likely coming from the decreased quality in the Aeolus data and does not represent any physical change in the regime. This suggests a strong temporal consistency in the general structure of the energy distribution

3.2 Zonal variation of GW activity from observations and ERA5

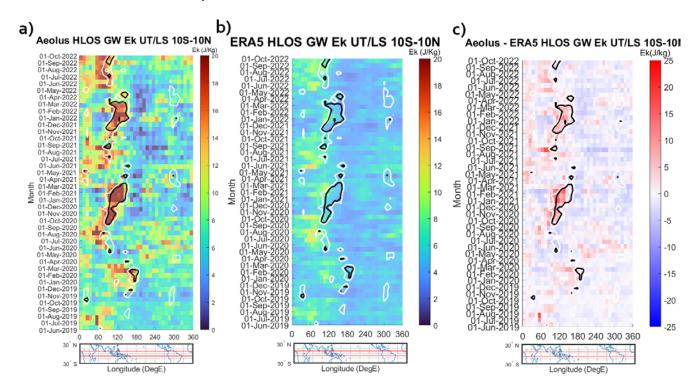


Figure 5. (a,b,c) Hovmoller diagram of $Ek_{Aeolus\,HLOS^*}$, $Ek_{ERA5\,HLOS}$ and their difference. The contour plot represents the Outgoing Longrange Radiation (OLR) for 210 and 220 W/m² (black and white, respectively). Each bin corresponds to an average of over 3 weeks and 10 degrees. The dark bins represent the lack of satellite information in (a). The OLR measurements were obtained from the Australian Bureau of Meteorology. The UTLS altitudes are defined between one kilometer below the tropopause and 22 km. The tropopause is determined from the NCEP reanalysis.

To assess the evolution and transition between the different seasons with greater precision, the Hovmoller diagrams in Fig.5 only show the observations between 10° N and 10° S, as Fig.4 proves this region contains most of the activity. Fig.5a shows $Ek_{Aeolus\,HLOS*}$, where a recurrent eastward propagation is seen multiple times above the Indian Ocean. This hotspot migrates from eastern Africa to the Pacific maritime continent between June and March. This shift is recurring over multiple years and shows a relative consistency between each year in terms of longitudinal and temporal range.





The presence of hotspots, represented by distinct shapes in the Ek patterns, is expected in regions with prevalent convective activity. These can be attributed to mechanisms responsible for convection-induced GWs. Deep convection in the atmosphere produces localized regions of intense upward motion and latent heat release. These convectively generated GWs can propagate vertically and interact with the large-scale atmospheric circulation, transferring momentum and energy to the background flow (Alexander et al., 2021).

We observe similar spatial and temporal patterns between $Ek_{Aeolus\,HLOS*}$ and the $Ek_{ERA5\,HLOS}$ shown in Fig.5b, with increased Ek values corresponding to low Outgoing Longwave Radiation (OLR) areas. The OLR represents the amount of terrestrial radiation released into space and, by extension, the amount of cloud cover and water vapor that intercepts that radiation in the atmosphere. Based on the findings in the study by Zhang et al. (2017), OLR serves as a reliable proxy for deep convection due to its strong correlation with diabatic heating and radiative tendencies. Hence, the correspondence between increased Ek values and OLR contours is unsurprising.

While the Aeolus and ERA5 Ek variations are generally consistent, the datasets show some discrepancies. In particular, as can be inferred from Fig.5c, ERA5 underestimates Ek in the regions of deep convection, characterized by lower OLR, suggesting a possible weakness of the reanalysis in resolving convection-induced wave activity.

4. Exploratory possibilities and limitations

4.1 Comparison with Potential Energy

While a conservative analysis might prioritize directly comparable metrics and cautious interpretations, exploring less conventional approaches can reveal patterns and relationships that remain hidden in traditional frameworks. One promising possibility of this study lies in comparing the kinetic energy of gravity waves observed by Aeolus with the potential energy derived from GNSS-RO data. GNSS-RO provides high-resolution temperature profiles that are used to estimate the potential energy of gravity waves. Previous studies that looked into GW climatology all relied on these estimate to base their observations on, as it was the only global instrumentation available (Schmidt et al., 2008; Alexander et al., 2008a; Šácha et al., 2014; Khaykin et al., 2015). Hence, we will adopt this method of comparison as well.



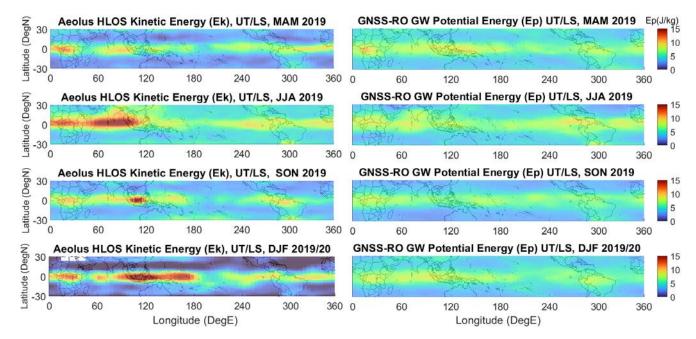


Figure 6. Comparison between $Ek_{Aeolus\,HLOS*}$ (left column) and Ep GNSSRO (right column). Each line corresponds to a season, from March-April-May 2019 to December-January-February 2021. The white bins represent the lack of satellite information. The UTLS altitudes are defined between one kilometer below the tropopause and 22 km. The tropopause is determined from the NCEP reanalysis.

Fig.6 offers a side-by-side seasonal comparison of Ek_{Aeolus HLOS*} (left column) and Ep derived from GNSS-RO (right column), covering the period from March 2019 to February 2021. The figure highlights key spatial and temporal patterns of gravity wave activity detected by each instrument, with both datasets presenting clear seasonal variability.

Although the ratios between Ek and Ep suggested by linear gravity wave theory generally range between 5/3 and 2.0, empirical observations show significant variability. This variability, which is influenced by geographical factors, nonlinear processes, or wave interactions, underscores the importance of examining these two forms of energy from different perspectives rather than seeking strict correspondences.

With that in mind, what stands out from this comparison is the overall consistency in detecting gravity wave hotspots, particularly within the tropical belt. One notable aspect of the comparison is the seasonal shift in gravity wave activity between the two datasets, with both detecting enhanced wave activity during certain months. Because of inherent differences (different line of sight and signal projection, different physical quantities and their varying ratio that is empirically challenging the literature, different signal treatment and correction), direct one-to-one comparisons are not appropriate. Nonetheless, it allows us to draw parallels with Aeolus observations, where spatial and temporal correlation of hotspots should follow the same





disposition, allowing for an independent benchmark. Despite these methodological differences, both instruments align on the seasonal peaks and general distribution of wave activity, reinforcing the reliability of the data.

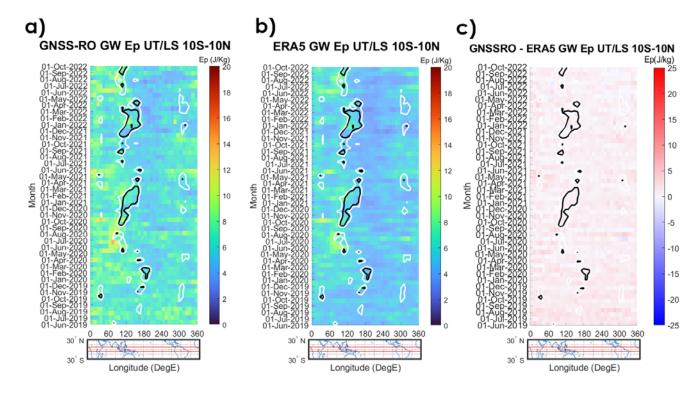


Figure 7. (a,b,c) Hovmoller diagram of $Ep_{GNSS-RO}$, Ep_{ERA5} and their difference. The contour plot represents the Outgoing Longrange Radiation (OLR) for 210 and 220 W/m² (black and white, respectively). Each bin corresponds to an average of over 3 weeks and 10 degrees. The OLR measurements were obtained from the Australian Bureau of Meteorology. The UTLS altitudes are defined between one kilometer below the tropopause and 22 km. The tropopause is determined from the NCEP reanalysis.

The Ep_{GNSS-Ro} shown in Fig.7a does not perfectly align with the structures described earlier, nor does it closely follow the patterns of OLR activity. As the method employed removes any traces of kelvin waves in the signal, the remaining activity is only comprised of GWs. This suggests that Ep does not effectively capture GW activity in regions of deep convection, as indicated by the lowest OLR values. However, it is found that the lesser convective areas are seen both on instances of Ek and Ep, in Fig.5a and Fig.7a (with notable examples such as August 2020 around 100°E, as well as in May 2021 and 2022 near 50°E). This observation supports the notion that, in terms of GW activity, deep convective phenomena primarily generate Ek, while less intense convective events (indicated in Fig.7a as occurring in the neighbouring region outside the white contours) produce a more balanced distribution between both energy components. It would be incorrect to assume that no wave activity occurs in low OLR regions; previous studies have shown that Ep values peak at 15 km altitude around the maritime continent, where the Walker circulation rises under non-El Niño conditions (Ern et al., 2004; Yang et al., 2021).



453

473



454 Nonetheless, the Ep_{ERA5} diagram shown in Fig.7b is very consistent with the results shown in Fig.7a, particularly in regions 455 outside the primary convection hotspots. For example, in August 2020 around 100°E, we see coherent signals in both datasets. 456 Similarly, in May 2021 near 50°E or in February 2022 near 120°E, distinct patterns emerge in both datasets. These alignments 457 458 indicate that when gravity waves have a stronger potential energy component, both datasets capture these features, even outside the primary zones of low OLR. It can also be noted that the patterns visible in Fig.7b strongly resemble the patterns presented 459 by ERA5 in Fig.5b, a sign of ERA5's tendency to rely on the existence of Ep to determine the presence of Ek. 460 461 462 The differences between ERA5 and GNSS-RO data, depicted in Fig.7c, are minimal and averaging at a 1.4 J/kg difference. 463 Given that ERA5 assimilates GNSS-RO data, that conclusion does not come as surprising. While ERA5 accurately represents 464 Ep in, and outside, of convective regions thanks to its assimilation of GNSS-RO data, the underestimation of Ek points to a specific limitation in capturing the kinetic energy component of convection-induced gravity waves. 465 466 467 This discrepancy then results from the absence of data from Aeolus or other instruments capable of retrieving similar wind-468 related information, as ERA5 mostly relies on geostrophic (thermal) winds in poorly wind-assimilated areas. This reliance on 469 derived wind data, rather than directly observed wind fields, could explain why ERA5 does not accurately capture the reality 470 observed by specialized instruments like Aeolus, which directly measure actual wind components. 471 472





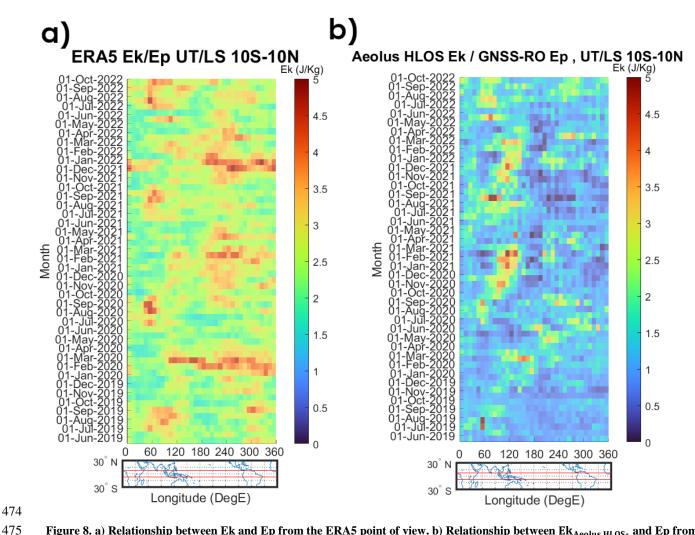


Figure 8. a) Relationship between Ek and Ep from the ERA5 point of view. b) Relationship between $Ek_{Aeolus\ HLOS*}$ and Ep from GNSSRO. The UTLS altitudes are defined between one kilometer below the tropopause and 22 km. The tropopause is determined from the NCEP reanalysis.

Fig. 8 presents a detailed analysis of the ratio between Ek and Ep from two perspectives: (a) from the ERA5 model and (b) comparing Aeolus's HLOS Ek and GNSS-RO-derived Ep. It illustrates the longitudinal and temporal variations of the Ek/Ep ratio across the equatorial band (10°S to 10°N) from June 2019 to October 2022.

When observed closely, a significant division between the Indian Ocean and the eastern Pacific, marked by a contrast around 180° longitude, can be noted in both figures. This contrast is not just a random occurrence but reflects underlying geographic factors, including orographic influences and convective activity. These two factors play a role in the generation and propagation of gravity waves, causing the distinct variations in the ratio between the two energies.





Figure 8a presents distinct hotspots in the Ek/Ep ratio, which could potentially arise from parametric noise or model assumptions. However, the alignment of these hotspots in Fig.8b, as observed by Aeolus and GNSS-RO, two independent instruments, (despite ERA5 assimilating GNSS-RO data) confirm the presence of these patterns. Notable examples include the series of hotspots included on the 60° to 120° longitude (July to September 2019, July 2020 to March 2021, July 2021 to March 2022 and July 2022 to October 2022) and another series of hotspots on the other side of the longitude range, at 200° to 260° longitude (February 2021 to March 2021 and December 2021 to March 2022). Since Aeolus provides energy metrics through a specific line of sight, we can conclude that the western activity mostly provides from zonal winds (where both patterns visually correspond), whereas the eastern activity probably contains a much stronger meridional component, explaining the weaker visual fidelity. In particular, the large red stripe in Fig. 8a during February–March 2020 comes from an intense intraseasonal disturbance, the 2020 Madden-Julian Oscillations (MJO), which can inject unusually strong gravity-wave energy into the upper troposphere (Kumari et al., 2021). The patterns on the western side of both figures show a pretty constant seasonality, and it could be argued that this is also the case for the eastern side patterns.

Upon further examination of the correlation between areas of maximum Ek/Ep ratios and the presence of dynamic hotspots, the data indicate a clear connection to regions of intense convective activity. This observation suggests that, in areas with similar seasonal characteristics, gravity waves tend to transport more kinetic energy during convective events, which amplifies their influence on the overall energy dynamics. The periodic patterns observed in the data also hint at a seasonal component previously observed by Zhang et al. (2010), potentially tied to atmospheric phenomena such as the shifting Intertropical Convergence Zone (ITCZ) or changes in jet stream dynamics (Hei et al., 2008). These seasonal fluctuations in the Ek/Ep ratio further reinforce the notion that gravity wave behavior is not static but is influenced by broader atmospheric cycles (Ern et al., 2018; Zhang et al., 2010), contrary to the traditional linear theory paradigm in the literature.

4.2 Vertical wavelength retrieval

Understanding the vertical wavelength of convective GWs is an essential element for characterizing their dynamics. However, Aeolus is inherently limited in retrieving accurate vertical wavelengths due to its design. The placement of range bins was fixed at the time of observation, introducing inconsistencies in vertical resolution that affect the precise identification of wave peaks and troughs. Additionally, the N/P parameter, which controls the number of accumulated measurements (N) and pulses (P) per cycle, introduces variability in the horizontal resolution of Aeolus data. Changes to this setting, such as the transition from N=30 to N=5, improve horizontal resolution but exacerbate the misrepresentation of vertical wave structures. These design limitations necessitate reliance on external datasets, such as ERA5, which provide a more continuous representation of vertical wave structures and finer-scale features.



516517

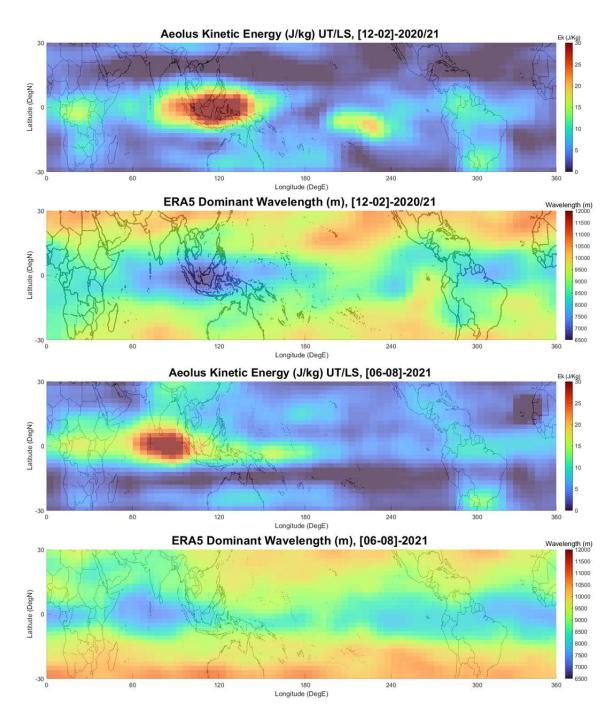


Figure 9. Comparison between $Ek_{Aeolus\ HLOS}$ * and the ERA5-retrieved wavelength for DJF 2020/21 and JJA 2021.





518

Figure 9 presents a comparison between $Ek_{Aeolus\ HLOS}$ * and the corresponding wavelengths retrieved from ERA5 during DJF

520 2020/21 and JJA 2021. In regions around convective spots, where Aeolus is shown to possess the highest EK, ERA5 displays

521 the lowest wavelength characteristics. This is expected, as waves with higher EK values are correlated with lower wavelengths.

Furthermore, gravity waves generated by convective processes often exhibit shorter horizontal wavelengths (Kalisch et al.,

523 2016), particularly those under 100 km, which poses a challenge for retrieval by instruments like Aeolus.

524

526

527

528

529

522

Waves with high EK are typically generated in regions with strong convective updrafts and downdrafts, where the rapid vertical

movement of air masses creates intense small-scale disturbances. These localized and transient disturbances, arising from

geostrophic imbalance, generate GWs that carry energy away from the convective region, where strong forcing efficiently

transfers energy into the EK spectrum at shorter wavelengths (Waite and Snyder, 2009). The correlation between high EK and

shorter wavelengths is particularly pronounced in convective systems, as confirmed in both observational and numerical

estimations (Kalisch et al., 2016), especially in tropical regions and cyclones (Chane Ming et al., 2014).

530531

532

533534

535

536

538

539

540

541

544

545

547

Sensitivity studies on ERA5 data, with and without Welch windowing and frequency filtering, showed that removing the

Welch windowing augmented overall values and produced less confined hotspots, suggesting spectral leakage. Without high-

pass frequency filtering (or low-pass wavelength filtering), the dominant wavelengths detected are significantly longer than

what Aeolus can resolve, reinforcing the necessity of filtering.

5. Discussion

537 Overall, the results presented in this study allow us to discuss and address two main questions. The first consistent observation

made, was that ERA5 underestimates Ek distribution in such regions compared to the Aeolus-derived energy, particularly over

the Indian Ocean, where conventional radiosonde wind measurements are very sparse. That difference raised questions on the

potential reason for such discrepancies: Is this result an overestimation of Aeolus, due to its known increased noise and

inconsistent performance during its life-cycle, or an underestimation for ERA5, due to the lack of direct wind observations

542 assimilated?

543 The analysis of ALADIN wind profiling and ECMWF ERA5 reanalysis data, provided in Fig. 4 and Fig. 5, revealed enhanced

GW activity over the Indian Ocean during Boreal Summer, as well as over the western Pacific and maritime continent in Boreal

Winter. The enhanced GW activity migrating from eastern Africa to the Pacific maritime continent between June and

546 December is linked to convection, as suggested by the correlation between enhanced GW Ek and the regional minima in OLR.

The relation between OLR and the MJO has been used before; It is a reliable index for analysis (Kiladis et al., 2014), hinting

548 towards the possibility for the active phase of the MJO to generate the observed hotspots through its convective activity. This



549

550

551

552

553

554

555

556557

558

559

560

561

562

563

564

565566

567

568

569570

571

572

573

574

575

576

577

578

579



suggests that Aeolus is effectively capturing convection-induced GWs that may be underrepresented in ERA5. One of the persistent features observed throughout the study was the high-energy gravity wave hotspot over the African continent, which remained consistent across seasons and years. This suggests a continuous mechanism of continental convection driving gravity wave activity in this region. An additional tool at our disposal to solve the case is the global distribution of Ep, through the use of independent GNSS-RO instruments. Our initial quarterly comparisons with GNSS-RO data, shown in Fig.6, revealed that Aeolus performs well, capturing similar values in the same regions all things considered, as these two results have a lot of inherent differences (different line of sight and signal projection, different physical quantities and their varying ratio, different signal treatment and correction). We also found that the assimilation is nearly perfect for Ep, with minimal discrepancies between ERA5 and GNSS-RO (see Fig.7c). The result does not come as surprising, as ERA5 assimilates GNSS-RO in great proportions but does not have any Aeolus data collected. This last hint proves that ERA5 shows no general difficulty at reproducing areas of convection when it has been exposed to enough data assimilation (Ep-driven convective areas in that case). Overall, the findings presented here are in full agreement with the elements outlined in the introduction, suggesting that ERA5 is underestimating the Ek component. Indeed, ERA5 has several known shortcomings, such as its underrepresentation of eastward-propagating inertio-gravity waves (Bramberger et al., 2022), its site-dependent errors in tropical regions (Campos et al., 2022), and the broader limitations of data assimilation systems in capturing circulation dynamics, particularly in areas with sparse wind observations (Podglajen et al., 2014; Žagar et al., 2004). These challenges are further emphasized by the QBO-MJO modulation of the wave activity in the UTLS, possibly at play in the amplitude variability of the seasonal signals seen in Fig.5a, where some years show an increased activity compared to others. An observational study revealed how gravity waves generated during MJO phases interact with QBO-modulated wind patterns, influencing their dissipation and energy dispersion (Kalisch et al., 2018). The QBO easterly phase (EQBO) has been shown to enhance MJO activity by strengthening convective signals and reinforcing the propagation of Rossby and Kelvin waves in the UTLS, while the westerly phase (WQBO) suppresses these dynamics (Song and Wu, 2020; Martin et al., 2021). However, the limitations of ERA5 in capturing QBO-MJO interactions are evident, as reanalysis datasets often fail to fully reproduce the observed temperature and wind anomalies associated with these processes, particularly in tropical regions (Lim and Son, 2022). Another discussion enabled by Aeolus observations concerns the longstanding assumption of a constant Ek/Ep ratio in GW studies. Specifically, the question arises: Is the conventional view of a constant ratio for inferring Ep from Ek (and vice versa) still tenable? Or do the new data suggest that this ratio is no longer universally valid in real-world, often non-linear, atmospheric conditions? At first glance, using a fixed ratio appears straightforward for converting well-documented Ep (from temperature-based



580

581

582

583

584

585

586

587588

589

590

591 592

593

594

595

596 597

598

599600

601

602

603 604

605

606 607

608

609



between 5/3 and 2.0 (VanZandt, 1985; Hei et al., 2008). In idealized models of linear wave behavior, the kinetic and potential energies are expected to be comparable, leading to a ratio close to unity. This has been confirmed previously, in a study such as Nastrom et al. (2000), which found that in stable, linear wave conditions, the energy ratios adhered closely to these theoretical predictions. However, a growing body of evidence challenges this simplification: Empirical work increasingly reveals significant variability in this ratio, indicating non-linear effects in real-world atmospheric conditions (Baumgarten et al., 2015; Guharay et al., 2010; Tsuda et al., 2004). When the observed energy ratios deviate significantly from this expected range, non-linear processes may be at play. For instance, in situations where wave amplitudes are particularly large, wave-wave interactions, such as those resulting from wave breaking or saturation, could lead to the observed discrepancies. This has been demonstrated in earlier work by Mack and Jay. (1967), who found that under certain conditions, potential energy deviated markedly from kinetic energy, suggesting non-linear effects. Similar findings have been reported by Fritts et al. (2009), who showed that interactions between gravity waves and fine atmospheric structures can result in turbulence, thereby affecting the balance between kinetic and potential energy. With everything in place to link these elements, the observed comparison in Fig. 8 of the Ek/Ep ratios from ERA5, Aeolus, and GNSS-RO confirms that the characteristics of gravity waves vary significantly across time and space. The observed ratios, 1.43 (+/- 0.76) for ERA5, 1.63 (+/- 0.7) for Aeolus/GNSS-RO, indicate that the waves encompass both linear and non-linear processes. The frequent observation of ratios exceeding unity, aligning with trends identified in previous studies, suggests that a substantial portion of the waves' energy is contained in kinetic form, often indicative of non-linear behavior. Because the assumption of a constant ratio is increasingly challenged by empirical observations, it accentuates the need to shift the paradigm from relying solely on temperature perturbations to directly deriving Ek. As such, directly measuring kinetic energy is, and has always been, a missing link for a comprehensive understanding of GW dynamics. Beyond these considerations of gravity wave dynamics and energy ratios, we should also acknowledge the limitations of the Aeolus satellite. These include both its technical shortcomings and the constraints imposed by its HLOS projection, which directly impact the representativeness of its measurements. A 1.6 ratio was determined for Ek/Ek_{HLOS} using ERA5, as seen in Fig.2. It reflects the efficiency with which HLOS winds from Aeolus can approximate the full kinetic energy field. The ratio indicates that HLOS winds account for approximately 62.5% of the total Ek, while the remaining 37.5% is undetectable due to the projection limitations of HLOS measurements. The discrepancy suggests that the HLOS winds alone cannot fully capture the energy contributions from multi-dimensional wave dynamics. However, this ratio can help estimate the full Ek indirectly with reasonable accuracy. While this approach introduces some assumptions, it can be further refined by cross-validating against comprehensive datasets from reanalyses like ERA5.



610 611

612

613

614

615 616

617

618

619

630

633 634

635

636

639



The spatial and temporal consistency observed between Aeolus and ERA5 datasets highlight the potential of Aeolus wind profiling for assimilation to improve our understanding of atmospheric dynamics in the tropical UTLS. However, there are limitations and uncertainties to consider; these include dark currents in its charge-coupled devices, known as "hot pixels", which can induce speed measurement errors of several meters per second (Weiler et al., 2021). Additionally, oscillating perturbations within the instrument can cause signal deformations, potentially misinterpreted as GW-induced signals (Ratynski et al., 2023). Even though corrections have been implemented, Fig.3 showed that the instrument's overall signal random error still fluctuates due to its degradation. While newer baselines such as the latest 2B16 used in this study, improve on the appearance rate of hot pixels, challenges remain in consistently identifying and correcting other issues such as oscillating perturbations, increased solar activity, or cloud contamination that can sporadically deform signals.

6. Conclusion

- 620 In this study, we examined the capacity of the Aeolus ALADIN instrument to capture and resolve GWs in tropical UTLS. 621 While this task might appear challenging at first, because of the data alteration issues Aeolus faced during its lifecycle, the
- 622 study proposed a noise correction process, which used ERA5 reanalysis as a reference to estimate and correct for Aeolus's
- instrument-induced variance. This correction improved the retrieving of kinetic energy, and our comparison with collocated 623
- radiosonde data further validated that approach. A key focus of our analysis was the ratio between kinetic and potential energies 624
- 625 (Ek/Ep), providing insights into the linear or non-linear nature of these waves. The wavelength retrieval aspect also emerged 626 as a limitation for Aeolus, reflecting constraints in the bin settings and horizontal integration of its HLOS wind measurements.
- The principal findings can be summarized as follows: 627
- Aeolus observations capture significant kinetic energy enhancements over tropical convection hotspots, particularly 628 629 over the Indian Ocean, where ERA5 shows substantial underrepresentation due to sparse wind observations.
- 631 Direct wind data from Aeolus could significantly enhance tropical UTLS reanalysis products, particularly in 632 convection-driven GW regimes, reducing biases in Ek representation.
 - In many regions with strong convective forcing, Aeolus data suggest a larger kinetic energy component, pointing to wave breaking, saturation, and other non-linear processes that depart from purely linear wave dynamics.
- While linear GW theory often prescribes an Ek/Ep ratio between ~1.6 and ~2.0, our results show that this ratio can 637 638 vary significantly, depending on location and season. This highlights the need for direct kinetic-energy measurements rather than relying solely on temperature-derived potential energy as a proxy.





 Aeolus also helps fill this gap. However, given its HLOS projection, Aeolus underestimates the total Ek if meridional components are significant, reinforcing that multi-instrument approaches are mandatory for accurately characterizing GW fields.

644 T

 Thus, this study has demonstrated the value of Aeolus Rayleigh wind profiling for observing GWs in the tropical UTLS, despite the high and time-variable random error associated with its measurements. Our findings confirm that the annual and zonal variation of GW activity in the tropical tropopause layer and lower stratosphere is modulated by deep convection, as demonstrated by Dzambo et al. (2019) and Evan et al. (2020). Furthermore, Aeolus data expose a significant need for improving the reanalysis regarding the convective GW Ek. The lack of GW-derived Ek in ERA5 is most pronounced in the Indian Ocean region, where conventional radiosonde wind measurements are relatively sparse. It is highly likely that the missing Ek in ERA5 is due to the misrepresentation of convective processes. The results also indicate that standard assumptions about the Ek/Ep ratio do not always hold, particularly under convective or otherwise non-linear conditions. Aeolus' range-bin design and horizontal integration restrict its ability to determine wavelengths with accuracy, which poses a significant challenge for fully capturing the characteristics of GW. This limitation highlights the need for complementary datasets, which could be addressed in newer iterations of the instrument. While this study delivers some insights into UTLS GW activity and the benefits of global wind observation, future research should continue investigating the factors contributing to the discrepancies observed between Aeolus and ERA5 data. Future missions like Aeolus-2 are expected to build on these findings,

Data Availability: Aeolus data are publicly available through the Aeolus online dissemination system (https://aeolus-ds.eo.esa.int/oads/access/). The dataset used for the realization of this study can be found at https://doi.org/10.5281/zenodo.8113261

Author Contributions: Conceptualization, M.R, S.K, A.H, and M.J.A; methodology, M.R, S.K, A.H, and M.J.A.; software, M.R. and A.M. .; validation, M.R, S.K, A.H, and M.J.A;—original draft preparation, M.R. and S.K. .; writing—review and editing, M.R, S.K, A.H, M.J.A, A.M, P.K and A.M; funding acquisition, S.K, P.K. and A.M; All authors have read and agreed to the published version of the manuscript.

Competing interests: The contact author has declared that none of the authors has any competing interests.

offering improved coverage and advancing our understanding of atmospheric dynamics.

Acknowledgments: The work by Mathieu Ratynski was carried out under a PhD fellowship co-funded by CNES and ACRIST. Additional funding has been provided via the CNES APR Aeolus project. MJA was funded by NSF grants #2110002 and
#1642644.





673 References

- 674 Alexander, M. J. and Ortland, D. A.: Equatorial waves in High Resolution Dynamics Limb Sounder (HIRDLS) data, J.
- 675 Geophys. Res. Atmospheres, 115, https://doi.org/10.1029/2010JD014782, 2010.
- 676 Alexander, M. J., Liu, C. C., Bacmeister, J., Bramberger, M., Hertzog, A., and Richter, J. H.: Observational Validation of
- 677 Parameterized Gravity Waves From Tropical Convection in the Whole Atmosphere Community Climate Model, J. Geophys.
- 678 Res. Atmospheres, 126, e2020JD033954, https://doi.org/10.1029/2020JD033954, 2021.
- 679 Alexander, S., Tsuda, T., and Kawatani, Y.: COSMIC GPS Observations of Northern Hemisphere winter stratospheric gravity
- 680 waves and comparisons with an atmospheric general circulation model, Geophys. Res. Lett. GEOPHYS RES LETT, 35,
- 681 https://doi.org/10.1029/2008GL033174, 2008a.
- 682 Alexander, S. P., Tsuda, T., and Kawatani, Y.: COSMIC GPS Observations of Northern Hemisphere winter stratospheric
- 683 gravity waves and comparisons with an atmospheric general circulation model, Geophys. Res. Lett., 35,
- 684 https://doi.org/10.1029/2008GL033174, 2008b.
- 685 Alexander, S. P., Tsuda, T., Kawatani, Y., and Takahashi, M.: Global distribution of atmospheric waves in the equatorial upper
- 686 troposphere and lower stratosphere: COSMIC observations of wave mean flow interactions, J. Geophys. Res. Atmospheres,
- 687 113, https://doi.org/10.1029/2008JD010039, 2008c.
- Baker, W. E., Atlas, R., Cardinali, C., Clement, A., Emmitt, G. D., Gentry, B. M., Hardesty, R. M., Källén, E., Kavaya, M. J.,
- 689 Langland, R., Ma, Z., Masutani, M., McCarty, W., Pierce, R. B., Pu, Z., Riishojgaard, L. P., Ryan, J., Tucker, S., Weissmann,
- 690 M., and Yoe, J. G.: Lidar-Measured Wind Profiles: The Missing Link in the Global Observing System, Bull. Am. Meteorol.
- 691 Soc., 95, 543–564, https://doi.org/10.1175/BAMS-D-12-00164.1, 2014.
- 692 Banyard, T. P., Wright, C. J., Hindley, N. P., Halloran, G., Krisch, I., Kaifler, B., and Hoffmann, L.: Atmospheric Gravity
- 693 Waves in Aeolus Wind Lidar Observations, Geophys. Res. Lett., 48, e2021GL092756,
- 694 https://doi.org/10.1029/2021GL092756, 2021.
- 695 Baumgarten, G., Fiedler, J., Hildebrand, J., and Lübken, F.-J.: Inertia gravity wave in the stratosphere and mesosphere observed
- 696 by Doppler wind and temperature lidar, Geophys. Res. Lett., 42, 10,929-10,936, https://doi.org/10.1002/2015GL066991, 2015.
- 697 Borne, M., Knippertz, P., Weissmann, M., Witschas, B., Flamant, C., Rios-Berrios, R., and Veals, P.: Validation of Aeolus
- 698 L2B products over the tropical Atlantic using radiosondes, Atmospheric Meas. Tech., 17, 561-581,
- 699 https://doi.org/10.5194/amt-17-561-2024, 2024.
- 700 Bramberger, M., Alexander, M. J., Davis, S., Podglajen, A., Hertzog, A., Kalnajs, L., Deshler, T., Goetz, J. D., and Khaykin,
- 701 S.: First Super-Pressure Balloon-Borne Fine-Vertical-Scale Profiles in the Upper TTL: Impacts of Atmospheric Waves on
- 702 Cirrus Clouds and the QBO, Geophys. Res. Lett., 49, e2021GL097596, https://doi.org/10.1029/2021GL097596, 2022.
- 703 Campos, R. M., Gramcianinov, C. B., de Camargo, R., and da Silva Dias, P. L.: Assessment and Calibration of ERA5 Severe
- Winds in the Atlantic Ocean Using Satellite Data, Remote Sens., 14, 4918, https://doi.org/10.3390/rs14194918, 2022.
- 705 Cao, B., Haase, J. S., Murphy, M. J., Alexander, M. J., Bramberger, M., and Hertzog, A.: Equatorial waves resolved by balloon-
- 5706 borne Global Navigation Satellite System radio occultation in the Strateole-2 campaign, Atmospheric Chem. Phys., 22, 15379—
- 707 15402, https://doi.org/10.5194/acp-22-15379-2022, 2022.





- 708 Chane Ming, F., Ibrahim, C., Barthe, C., Jolivet, S., Keckhut, P., Liou, Y.-A., and Kuleshov, Y.: Observation and a numerical
- 709 study of gravity waves during tropical cyclone Ivan (2008), Atmospheric Chem. Phys., 14, 641-658,
- 710 https://doi.org/10.5194/acp-14-641-2014, 2014.
- 711 Danzer, J., Pieler, M., and Kirchengast, G.: Closing the gap in the tropics: the added value of radio-occultation data for wind
- 712 field monitoring across the equator, Atmospheric Meas. Tech. Discuss., 1–19, https://doi.org/10.5194/amt-2023-137, 2023.
- 713 Dhaka, S. K., Yamamoto, M. K., Shibagaki, Y., Hashiguchi, H., Fukao, S., and Chun, H.-Y.: Equatorial Atmosphere Radar
- 714 observations of short vertical wavelength gravity waves in the upper troposphere and lower stratosphere region induced by
- 715 localized convection, Geophys. Res. Lett., 33, https://doi.org/10.1029/2006GL027026, 2006.
- 716 Dzambo, A. M., Hitchman, M. H., and Chang, K.-W.: The Influence of Gravity Waves on Ice Saturation in the Tropical
- 717 Tropopause Layer over Darwin, Australia, Atmosphere, 10, 778, https://doi.org/10.3390/atmos10120778, 2019.
- 718 Ern, M., Preusse, P., Alexander, M. J., and Warner, C. D.: Absolute values of gravity wave momentum flux derived from
- 719 satellite data, J. Geophys. Res. Atmospheres, 109, https://doi.org/10.1029/2004JD004752, 2004.
- 720 Ern, M., Trinh, Q. T., Preusse, P., Gille, J. C., Mlynczak, M. G., Russell III, J. M., and Riese, M.: GRACILE: a comprehensive
- 721 climatology of atmospheric gravity wave parameters based on satellite limb soundings, Earth Syst. Sci. Data, 10, 857–892,
- 722 https://doi.org/10.5194/essd-10-857-2018, 2018.
- 723 Evan, S., Brioude, J., Rosenlof, K., Davis, S. M., Vömel, H., Héron, D., Posny, F., Metzger, J.-M., Duflot, V., Payen, G.,
- 724 Vérèmes, H., Keckhut, P., and Cammas, J.-P.: Effect of deep convection on the tropical tropopause layer composition over the
- southwest Indian Ocean during austral summer, Atmospheric Chem. Phys., 20, 10565–10586, https://doi.org/10.5194/acp-20-
- 726 10565-2020, 2020.
- 727 Fritts, D. C. and Alexander, M. J.: Gravity wave dynamics and effects in the middle atmosphere, Rev. Geophys., 41,
- 728 https://doi.org/10.1029/2001RG000106, 2003.
- 729 Fritts, D. C., Wang, L., and Werne, J.: Gravity wave-fine structure interactions: A reservoir of small-scale and large-scale
- 730 turbulence energy, Geophys. Res. Lett., 36, https://doi.org/10.1029/2009GL039501, 2009.
- 731 Fröhlich, K., Schmidt, T., Ern, M., Preusse, P., de la Torre, A., Wickert, J., and Jacobi, Ch.: The global distribution of gravity
- 732 wave energy in the lower stratosphere derived from GPS data and gravity wave modelling: Attempt and challenges, J.
- 733 Atmospheric Sol.-Terr. Phys., 69, 2238–2248, https://doi.org/10.1016/j.jastp.2007.07.005, 2007.
- 734 Geldenhuys, M., Kaifler, B., Preusse, P., Ungermann, J., Alexander, P., Krasauskas, L., Rhode, S., Woiwode, W., Ern, M.,
- 735 Rapp, M., and Riese, M.: Observations of Gravity Wave Refraction and Its Causes and Consequences, J. Geophys. Res.
- 736 Atmospheres, 128, e2022JD036830, https://doi.org/10.1029/2022JD036830, 2023.
- 737 Gubenko, V. N., Pavelyev, A. G., Salimzyanov, R. R., and Andreev, V. E.: A method for determination of internal gravity
- 738 wave parameters from a vertical temperature or density profile measurement in the Earth's atmosphere, Cosm. Res., 50, 21-
- 739 31, https://doi.org/10.1134/S0010952512010029, 2012.
- 740 Guharay, A., Venkat Ratnam, M., Nath, D., and Dumka, U. C.: Investigation of saturated gravity waves in the tropical lower
- 741 atmosphere using radiosonde observations, Radio Sci., 45, https://doi.org/10.1029/2010RS004372, 2010.
- 742 Hei, H., Tsuda, T., and Hirooka, T.: Characteristics of atmospheric gravity wave activity in the polar regions revealed by GPS
- radio occultation data with CHAMP, J. Geophys. Res. Atmospheres, 113, https://doi.org/10.1029/2007JD008938, 2008.





- Hersbach, H., Bell, B., Berrisford, P., Hirahara, S., Horányi, A., Muñoz-Sabater, J., Nicolas, J., Peubey, C., Radu, R., Schepers,
- 745 D., Simmons, A., Soci, C., Abdalla, S., Abellan, X., Balsamo, G., Bechtold, P., Biavati, G., Bidlot, J., Bonavita, M., De Chiara,
- 746 G., Dahlgren, P., Dee, D., Diamantakis, M., Dragani, R., Flemming, J., Forbes, R., Fuentes, M., Geer, A., Haimberger, L.,
- 747 Healy, S., Hogan, R. J., Hólm, E., Janisková, M., Keeley, S., Laloyaux, P., Lopez, P., Lupu, C., Radnoti, G., de Rosnay, P.,
- 748 Rozum, I., Vamborg, F., Villaume, S., and Thépaut, J.-N.: The ERA5 global reanalysis, Q. J. R. Meteorol. Soc., 146, 1999–
- 749 2049, https://doi.org/10.1002/qj.3803, 2020.
- Holloway, C. E. and Neelin, J. D.: The Convective Cold Top and Quasi Equilibrium, https://doi.org/10.1175/JAS3907.1, 2007.
- 751 John, S. R. and Kumar, K. K.: A discussion on the methods of extracting gravity wave perturbations from space-based
- 752 measurements, Geophys. Res. Lett., 40, 2406–2410, https://doi.org/10.1002/grl.50451, 2013.
- 753 Kalisch, S., Chun, H.-Y., Ern, M., Preusse, P., Trinh, Q. T., Eckermann, S. D., and Riese, M.: Comparison of simulated and
- 754 observed convective gravity waves, J. Geophys. Res. Atmospheres, 121, 13,474-13,492,
- 755 https://doi.org/10.1002/2016JD025235, 2016.
- 756 Kalisch, S., Kang, M.-J., and Chun, H.-Y.: Impact of Convective Gravity Waves on the Tropical Middle Atmosphere During
- 757 the Madden-Julian Oscillation, J. Geophys. Res. Atmospheres, 123, 8975–8992, https://doi.org/10.1029/2017JD028221, 2018.
- 758 Khaykin, S. M., Hauchecorne, A., Mzé, N., and Keckhut, P.: Seasonal variation of gravity wave activity at midlatitudes from
- 759 7 years of COSMIC GPS and Rayleigh lidar temperature observations, Geophys. Res. Lett., 42, 1251–1258,
- 760 https://doi.org/10.1002/2014GL062891, 2015.
- 761 Kiladis, G., Dias, J., Straub, K., Wheeler, M., Tulich, S., Kikuchi, K., Weickmann, K., and Ventrice, M.: A Comparison of
- 762 OLR and Circulation-Based Indices for Tracking the MJO, Mon. Weather Rev., 142, 1697-1715,
- 763 https://doi.org/10.1175/MWR-D-13-00301.1, 2014.
- 764 Kim, J.-E. and Alexander, M. J.: Direct impacts of waves on tropical cold point tropopause temperature, Geophys. Res. Lett.,
- 765 42, 1584–1592, https://doi.org/10.1002/2014GL062737, 2015.
- 766 Kumari, K., Wu, H., Long, A., Lu, X., and Oberheide, J.: Mechanism Studies of Madden-Julian Oscillation Coupling Into the
- Mesosphere/Lower Thermosphere Tides Using SABER, MERRA-2, and SD-WACCMX, J. Geophys. Res. Atmospheres, 126,
- 768 e2021JD034595, https://doi.org/10.1029/2021JD034595, 2021.
- 769 Ladstädter, F., Steiner, A. K., Foelsche, U., Haimberger, L., Tavolato, C., and Kirchengast, G.: An assessment of differences
- 770 in lower stratospheric temperature records from (A)MSU, radiosondes, and GPS radio occultation, Atmospheric Meas. Tech.,
- 771 4, 1965–1977, https://doi.org/10.5194/amt-4-1965-2011, 2011.
- 772 Lim, Y. and Son, S.-W.: OBO Wind Influence on MJO-Induced Temperature Anomalies in the Upper Troposphere and Lower
- 773 Stratosphere in an Idealized Model, https://doi.org/10.1175/JAS-D-21-0296.1, 2022.
- 774 Luna, D., Alexander, P., and de la Torre, A.: Evaluation of uncertainty in gravity wave potential energy calculations through
- 775 GPS radio occultation measurements, Adv. Space Res., 52, 879–882, https://doi.org/10.1016/j.asr.2013.05.015, 2013.
- 776 Mack, L. R. and Jay, B. E.: The partition of energy in standing gravity waves of finite amplitude, J. Geophys. Res. 1896-1977,
- 777 72, 573–581, https://doi.org/10.1029/JZ072i002p00573, 1967.
- 778 MARQUARDT, C. and Healy, S.: Measurement Noise and Stratospheric Gravity Wave Characteristics Obtained from GPS
- 779 Occultation Data, J. Meteorol. Soc. Jpn. J METEOROL SOC JPN, 83, 417–428, https://doi.org/10.2151/jmsj.83.417, 2005.





- 780 Martin, Z., Son, S.-W., Butler, A., Hendon, H., Kim, H., Sobel, A., Yoden, S., and Zhang, C.: The influence of the quasi-
- biennial oscillation on the Madden–Julian oscillation, Nat. Rev. Earth Environ., 2, 477–489, https://doi.org/10.1038/s43017-
- 782 021-00173-9, 2021.
- 783 Munday, C., Engelstaedter, S., Ouma, G., Ogutu, G., Olago, D., Ong'ech, D., Lees, T., Wanguba, B., Nkatha, R., Ogolla, C.,
- 784 Gàlgalo, R. A., Dokata, A. J., Kirui, E., Hope, R., and Washington, R.: Observations of the Turkana Jet and the East African
- 785 Dry Tropics: The RIFTJet Field Campaign, Bull. Am. Meteorol. Soc., 103, E1828–E1842, https://doi.org/10.1175/BAMS-D-
- 786 21-0214.1, 2022.
- 787 Muñoz-Sabater, J., Dutra, E., Agustí-Panareda, A., Albergel, C., Arduini, G., Balsamo, G., Boussetta, S., Choulga, M.,
- Harrigan, S., Hersbach, H., Martens, B., Miralles, D. G., Piles, M., Rodríguez-Fernández, N. J., Zsoter, E., Buontempo, C.,
- 789 and Thépaut, J.-N.: ERA5-Land: a state-of-the-art global reanalysis dataset for land applications, Earth Syst. Sci. Data, 13,
- 790 4349–4383, https://doi.org/10.5194/essd-13-4349-2021, 2021.
- 791 Nastrom, G. D., Hansen, A. R., Tsuda, T., Nishida, M., and Ware, R.: A comparison of gravity wave energy observed by VHF
- 792 radar and GPS/MET over central North America, J. Geophys. Res. Atmospheres, 105, 4685-4687,
- 793 https://doi.org/10.1029/1999JD901164, 2000.
- 794 Plougonven, R. and Zhang, F.: Internal gravity waves from atmospheric jets and fronts, Rev. Geophys., 52, 33-76,
- 795 https://doi.org/10.1002/2012RG000419, 2014.
- 796 Podglajen, A., Hertzog, A., Plougonven, R., and Žagar, N.: Assessment of the accuracy of (re)analyses in the equatorial lower
- 797 stratosphere, J. Geophys. Res. Atmospheres, 119, 11,166-11,188, https://doi.org/10.1002/2014JD021849, 2014.
- 798 Ratynski, M., Khaykin, S., Hauchecorne, A., Wing, R., Cammas, J.-P., Hello, Y., and Keckhut, P.: Validation of Aeolus wind
- 799 profiles using ground-based lidar and radiosonde observations at Réunion island and the Observatoire de Haute-Provence,
- 800 Atmospheric Meas. Tech., 16, 997–1016, https://doi.org/10.5194/amt-16-997-2023, 2023.
- 801 Rennie, M. P. and Isaksen, L.: The NWP impact of Aeolus level-2B winds at ECMWF, ECMWF Technical Memorandum
- 802 864, https://doi.org/10.21957/alift7mhr, 2020.
- 803 Rennie, M. P., Isaksen, L., Weiler, F., Jos de Kloe, Kanitz, T., and Reitebuch, O.: The impact of Aeolus wind retrievals on
- 804 ECMWF global weather forecasts, Q. J. R. Meteorol. Soc., 147, 3555–3586, https://doi.org/10.1002/qj.4142, 2021.
- 805 Šácha, P., Foelsche, U., and Pišoft, P.: Analysis of internal gravity waves with GPS RO density profiles, Atmospheric Meas.
- 806 Tech., 7, 4123–4132, https://doi.org/10.5194/amt-7-4123-2014, 2014.
- 807 Schmidt, T., de la Torre, A., and Wickert, J.: Global gravity wave activity in the tropopause region from CHAMP radio
- 808 occultation data, Geophys. Res. Lett., 35, https://doi.org/10.1029/2008GL034986, 2008.
- 809 Schmidt, T., Alexander, P., and de la Torre, A.: Stratospheric gravity wave momentum flux from radio occultations, J.
- 810 Geophys. Res. Atmospheres, 121, 4443–4467, https://doi.org/10.1002/2015JD024135, 2016.
- 811 Song, L. and Wu, R.: Modulation of the Westerly and Easterly Quasi-Biennial Oscillation Phases on the Connection between
- the Madden–Julian Oscillation and the Arctic Oscillation, Atmosphere, 11, 175, https://doi.org/10.3390/atmos11020175, 2020.
- 813 Stephan, C. C. and Mariaccia, A.: The signature of the tropospheric gravity wave background in observed mesoscale motion,
- 814 Weather Clim. Dyn., 2, 359–372, https://doi.org/10.5194/wcd-2-359-2021, 2021.





- 815 Tsuda, T., Nishida, M., Rocken, C., and Ware, R. H.: A Global Morphology of Gravity Wave Activity in the Stratosphere
- 816 Revealed by the GPS Occultation Data (GPS/MET), J. Geophys. Res. Atmospheres, 105, 7257–7273,
- 817 https://doi.org/10.1029/1999JD901005, 2000.
- 818 Tsuda, T., Ratnam, M. V., May, P. T., Alexander, M. J., Vincent, R. A., and MacKinnon, A.: Characteristics of gravity waves
- 819 with short vertical wavelengths observed with radiosonde and GPS occultation during DAWEX (Darwin Area Wave
- 820 Experiment), J. Geophys. Res. Atmospheres, 109, https://doi.org/10.1029/2004JD004946, 2004.
- 821 VanZandt, T. E.: A model for gravity wave spectra observed by Doppler sounding systems, Radio Sci., 20, 1323–1330,
- 822 https://doi.org/10.1029/RS020i006p01323, 1985.
- 823 Waite, M. L. and Snyder, C.: The Mesoscale Kinetic Energy Spectrum of a Baroclinic Life Cycle,
- 824 https://doi.org/10.1175/2008JAS2829.1, 2009.
- 825 Wang, L. and Alexander, M. J.: Global estimates of gravity wave parameters from GPS radio occultation temperature data, J.
- 826 Geophys. Res. Atmospheres, 115, https://doi.org/10.1029/2010JD013860, 2010.
- 827 Weiler, F., Kanitz, T., Wernham, D., Rennie, M., Huber, D., Schillinger, M., Saint-Pe, O., Bell, R., Parrinello, T., and
- 828 Reitebuch, O.: Characterization of dark current signal measurements of the ACCDs used on board the Aeolus satellite,
- 829 Atmospheric Meas. Tech., 14, 5153–5177, https://doi.org/10.5194/amt-14-5153-2021, 2021.
- 830 Wright, C. J. and Hindley, N. P.: How well do stratospheric reanalyses reproduce high-resolution satellite temperature
- 831 measurements?, Atmospheric Chem. Phys., 18, 13703–13731, https://doi.org/10.5194/acp-18-13703-2018, 2018.
- 832 Wüst, S. and Bittner, M.: Gravity wave reflection: Case study based on rocket data, J. Atmospheric Sol.-Terr. Phys., 70, 742–
- 833 755, https://doi.org/10.1016/j.jastp.2007.10.010, 2008.
- 834 Yang, S.-S., Pan, C.-J., and Das, U.: Investigating the Spatio-Temporal Distribution of Gravity Wave Potential Energy over
- the Equatorial Region Using the ERA5 Reanalysis Data, Atmosphere, 12, 311, https://doi.org/10.3390/atmos12030311, 2021.
- 836 Žagar, N., Gustafsson, N., and Källén, E.: Variational data assimilation in the tropics: The impact of a background-error
- 837 constraint, Q. J. R. Meteorol. Soc., 130, 103–125, https://doi.org/10.1256/qj.03.13, 2004.
- 838 Zhang, K., Randel, W. J., and Fu, R.: Relationships between outgoing longwave radiation and diabatic heating in reanalyses,
- 839 Clim. Dyn., 49, 2911–2929, https://doi.org/10.1007/s00382-016-3501-0, 2017.
- 840 Zhang, S. D. and Yi, F.: A statistical study of gravity waves from radiosonde observations at Wuhan (30° N, 114° E) China,
- 841 Ann. Geophys., 23, 665–673, https://doi.org/10.5194/angeo-23-665-2005, 2005.
- 842 Zhang, S. D., Yi, F., Huang, C. M., and Zhou, Q.: Latitudinal and seasonal variations of lower atmospheric inertial gravity
- 843 wave energy revealed by US radiosonde data, Ann. Geophys., 28, 1065–1074, https://doi.org/10.5194/angeo-28-1065-2010,
- 844 2010.

845